A&A 383, 881–891 (2002)
DOI: 10.1051/0004-6361:20020049

Astronomy & Astrophysics

UVSTAR observations of Adara (ϵ CMa): 575–1250 Å

A. Gregorio[1,2], R. Stalio[1,2], L. Broadfoot[3], F. Castelli[4], M. Hack[1], and J. Holberg[3]

[1] Dipartimento di Astronomia, Università di Trieste, 34131 Trieste, Italy
[2] Center for Advanced Research in Space Optics, Area Science Park, 34012 Trieste, Italy
[3] Department of Planetary Sciences, Lunar and Planetary Laboratory, University of Arizona, Tucson, AZ 85721, USA
[4] CNR-IAS and Osservatorio Astronomico di Trieste, 34131 Trieste, Italy

Received 13 November 2000 / Accepted 10 December 2001

Abstract. UVSTAR, UltraViolet Spectrograph Telescope for Astronomical Research, operates in the 500–1250 Å wave-band at 1 to 3 Å resolution. Here we report on the EUV and FUV observations of the B2 II star Adara, the brightest EUV source in the sky, obtained by UVSTAR during the STS 69 and STS 95 missions. The discussion concerns 1) wavelength and flux calibration, 2) short term time variability of selected spectral features, 3) comparison with previous measurements in the EUV band and 4) comparison with model atmospheres.

Key words. stars: individual: ϵ CMa – early-type – oscillations – ultraviolet: stars – instrumentation: spectrographs – space vehicles

1. Introduction

Adara (ϵ Canis Majoris, HD 52089, HR 2618) is among the most widely and comprehensively studied stars, from the Infrared to the X–Ray band. It is a m_V=1.5 B2 II star and an MK standard. The distance is 132^{+11}_{-9} pc (ESA 1997). The angular diameter was measured with an intensity interferometer as $(0.80 \pm 0.05) \times 10^{-3}$ arcsec (Hanbury Brown et al. 1974) which corresponds to a radius of $(11.4 \pm 0.7)\ R_\odot$. It is reported by Struve & Zebergs (1960) to be a non-variable B2 II giant. Other parameters of Adara are given in Table 1.

Table 1. Adara parameters.

	Data
$T_{\rm eff}$ (Code et al. 1976)	(20990 ± 750) K
$\log g$ (Hoare et al. 1993)	3.20 ± 0.15
$v \sin i$ (Uesugi & Fukuda 1982)	35 km s^{-1}
$\mathrm{d}M/\mathrm{d}t$ (Drew et al. 1994)	$\simeq 1 \times 10^{-8}\ M_\odot$/year

Adara is the brightest Extreme UltraViolet source in the sky (Bowyer et al. 1996): longward of 300 Å its EUV spectrum is about 30 times more intense than that of other stars having comparable distance and comparable flux for $\lambda > 911$ Å (e.g. the white dwarf HZ 43, Kruk et al. 1997). This large EUV flux should be mainly due to the extremely low neutral hydrogen column density in the direction of Adara. According to Gry et al. (1995) the density is of the order of 5×10^{17} atoms cm^{-2}, i.e. from three to five orders of magnitude lower than the average density of the Local Interstellar Medium in other directions (Welsh 1991; Gry et al. 1985). According to Cassinelli et al. (1995), Adara is situated in a rarefied interstellar tunnel, 300 pc long with about 50 pc diameter, which could be an extension of the Local Bubble region surrounding the Sun. According to Vallerga & Welsh (1996), the contribution of Adara to the local interstellar hydrogen ionization is such that it produces more hydrogen ionizing flux than all nearby stars combined. Among them β CMa, situated close to Adara, is the second brightest EUV source.

The most recent observations of Adara in the extreme UV are those from the EUVE experiment at a resolution $\lambda/\Delta\lambda$ of about 250 (Cassinelli et al. 1995) and those obtained with the ORFEUS-SPS II experiment at a resolution $\lambda/\Delta\lambda$ of about 1250 (Cohen et al. 1998). EUVE observations cover the range 300–740 Å, while ORFEUS observations cover the range 520–665 Å. Furthermore, observations of Adara from 500 Å to 700 Å were performed by the Voyager experiment at a resolution $\lambda/\Delta\lambda$ of about 55.

In this paper we present new observations of Adara at a resolution $\lambda/\Delta\lambda \sim 300$, obtained with the UVSTAR (Ultraviolet Spectrograph Telescope for Astronomical Research) experiment (Sandel et al. 1993; Stalio et al. 1999; Stalio & Gregorio 2000; De Carlo et al. 1994; Trampus et al. 1999a, 1999b). The observations extend from 500 Å to 1250 Å, so filling in the gap between 740 Å

and 900 Å in spectra observed at resolutions larger than 250. The wide wavelength range and the intermediate resolution of the UVSTAR spectra of Adara are good reasons for assuming that new information can be extracted from the far and extreme ultraviolet.

2. FUV and EUV spectra

2.1. Previous observations

The Voyager UVS spectrographs observed Adara from 500 to 1700 Å at low resolution. No EUV signal was detected due to the faintness of the EUV flux as compared to the scattered FUV flux (Holberg et al. 1991).

EUVE (Cassinelli et al. 1995) observed the EUV spectrum in the band 500–730 Å at an average resolution $\lambda/\Delta\lambda$ of the order of 250. The spectra were calibrated in absolute flux unit. This was the first spectrophotometric EUV observation of Adara which pointed out the difficulty of classical model atmospheres in reproducing the Adara spectrum shortward of the Lyman discontinuity.

The ORFEUS-SPAS II mission provided high resolution spectra ($\Delta\lambda/\lambda \simeq 1250$) in the EUV band 370–695 Å (Cohen et al. 1998). This was the first high resolution measurement in the EUV band and the quality of the spectra allowed to identify most of the line features, compare them with models and examine some wind broadened lines of O V and Si IV. ORFEUS-SPAS II data are not calibrated in absolute flux units, but the flux level was estimated to be about three times that from EUVE.

2.2. UVSTAR observations

UVSTAR, UltraViolet Spectrograph Telescope for Astronomical Research operates in the 500–1250 Å wave-band at 1 to 3 Å spectral resolutions. It consists of a movable platform providing fine pointing and two optical systems, the EUV and the FUV channels operating at wavelengths from 535 to 935 Å from 850 to 1250 Å, respectively.

UVSTAR has flown as a Hitchhiker–M payload on the STS 69 mission (September 7–18, 1995), STS 85 (August 7–19, 1997) and STS 95 (October 29–November 7, 1998), the first three of a series of five flights that NASA has allocated to the IEH (International Extreme–ultraviolet Hitchhiker) program.

UVSTAR observed Adara both during the STS 69 and STS 95 missions. In the latter mission Adara was observed both in the EUV and in the FUV bands.

2.2.1. STS 69: FUV

During the STS 69 mission a mechanical failure prevented UVSTAR from tracking in elevation. When observing Adara, the integration time was kept at five seconds in order to reduce the effect of Shuttle oscillations and the consequent loss of spectral resolution and light.

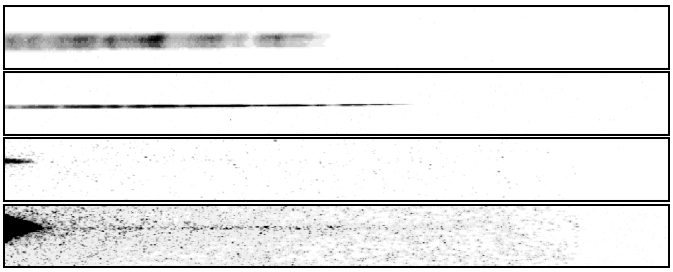

Fig. 1. Four Adara images by UVSTAR: a STS 69 FUV image (top panel), a STS 95 FUV image (second panel) and two STS 95 EUV images at different intensifier gains (last two panels) as a function of the wavelength (1024 pixels along the horizontal axis: longer wavelengths are on the left); the cross dispersion direction gives the spatial coordinate.

In Fig. 1 (top panel) we present one of the images obtained. Between MET (Mission Elapsed Time) 08/04:16 and 08/10:25 UVSTAR obtained 53 FUV images and no EUV images.

2.2.2. STS 95: EUV, FUV

During the STS 95 mission Adara was observed twice. The first observation (MET 01/19:55–01/20:10) was only used for instrument calibration and FUV channel alignment. The second observation (MET 06/04:26–06/05:21) allowed the EUV channel alignment and science observations. The alignment was obtained by shifting the EUV long wavelength limit to about 935 Å to include part of the FUV spectrum for fast signal detection. The acquired science data consists of 55 FUV and 22 EUV spectra.

Figure 1 displays three examples of STS 95 observations. Each image corresponds to the sum of three frames with an integration time of about five seconds per frame for a total integration time of 16 s. The second panel shows a typical FUV image with signal to noise ratio of about 20. The last two panels show integrated EUV spectra taken at different intensifier gains. One notices how difficult it is to obtain high quality EUV data near a strong FUV source of scattered light. In fact, the third panel represents an example of too low a gain while the last panel shows a reasonable compromise between FUV saturation and EUV signal/background ratio. For this analysis only this last type of images has been used (nine spectra) while the low gain images have been used for wavelength calibration; note that some EUV spectra have not been used due to the poor quality of the data.

3. Calibration

3.1. Wavelength calibration

The wavelength calibration in the FUV channel (850–1250 Å) was performed by identifying the stronger absorption lines. The lines at 1128.3, 1175.5 and 1206.6 Å corresponding to Si IV, C III and Si III respectively, were used. Figure 2 shows the STS 95 FUV spectrum obtained

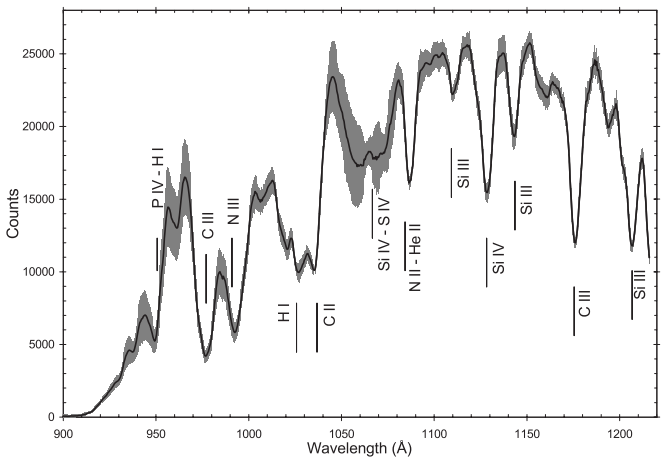

Fig. 2. The STS 95 FUV spectrum with the identification of major spectral features. The band represents the dispersion of the high quality data.

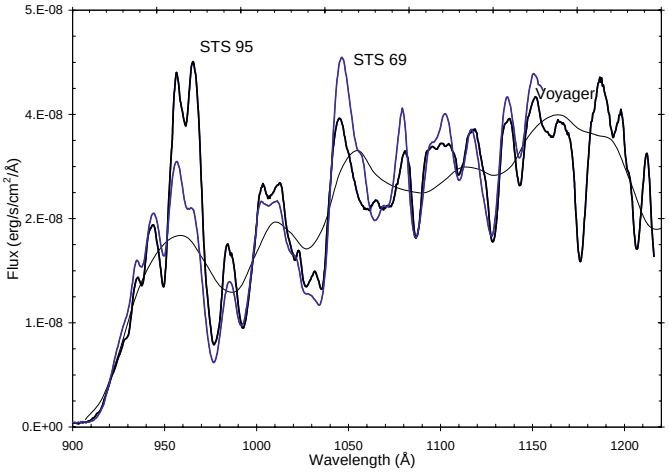

Fig. 3. The calibrated STS 69 and STS 95 UVSTAR spectra (thick lines, grey and black respectively) compared with Voyager spectrum (thin line).

by averaging the high quality spectra (an analysis has limited to 38 out of 55 the number of high quality spectra). The error band has been determined by evaluating the standard deviation among the spectra, the statistical error on the mean is this band times $1/\sqrt{38}$.

The in-flight wavelength calibration in the EUV channel (535–935 Å) was performed by using the mutual overlap between the two UVSTAR channels in the band 900–935 Å. Due to the high FUV signal intensity, which causes a saturation in the long wavelength region of the EUV channel, nine chosen EUV spectra with low gain (third panel in Fig. 1) were used. A further check on the wavelength calibration of the EUV channel is provided by observation of Jupiter Io Torus (Broadfoot 2000). We have estimated an error on the EUV channel wavelength calibration of ±2 pixel corresponding to about ±0.9 Å.

3.2. Flux calibration, FUV

In order to be compared, the STS 69 and STS 95 spectra have been corrected for the different detector sensitivity. Absolute flux calibration was then performed by means of the Voyager UVS calibrated fluxes of Adara (Holberg et al. 1991). The Voyager absolute flux calibration has been cross-checked with other instruments such as HUT Astro-1 (Kruk et al. 1997; Buss et al. 1994) and EURD (Morales et al. 2000; Morales et al. 2001). Voyager and HUT agree within 10%, Voyager and EURD data are consistent. The derived calibration curve matches the one derived for BD +28° 4211 (Stalio & Gregorio 2000). Figure 3 shows the resulting spectra. The uncertainty in the absolute flux level is estimated to be of the order of 15%.

3.3. Flux calibration, EUV

We have developed a technique capable of calibrating, to a first approximation, the EUV spectrum. Due to the wavelength superposition between the two channels, the EUV band extends above the Lyman limit at 912 Å: the level of the FUV flux is about 400 times larger than the EUV flux and produces a large amount of scattered light due to detector saturation effects (see last panel in Fig. 1 on the left). This light is maximum at the long wavelength part and at the center of the image. The amount of scattered light has been evaluated on each image by extrapolating its level from the behaviour in the strips above and below the stellar spectrum. Nine cleaned EUV stellar spectra have been obtained by subtracting the derived scattered light distribution. The quality has been furtherly improved by excluding from the set of nine values that value which makes the standard deviation decrease for each of the 1024 pixels. The remaining values have been averaged, standard deviations of the mean represent the errors.

The EUV and FUV detectors are the same apart the gain which during the Adara observation has been set to different but known values. The FUV flux calibration, corrected for the different gains, has been extrapolated to the EUV channel. We have checked the behaviour of the EUV and FUV calibrated spectra in the superposition region (800–900 Å) and corrected for a factor of 1.3 due to a known slightly different efficiency of the detectors. This procedure, although crude, allows us to determine a complete Adara spectrum over the wavelength band from 575 to 1250 Å (below 575 Å the detector sensitivity is too low).

Figure 4 compares the UVSTAR spectrum absolutely calibrated with the EUVE spectrum made available to us by D. Cohen. The different behaviour of two observed fluxes is evident. Figure 5 compares the spectra observed by UVSTAR, EUVE, and ORFEUS normalized to the pseudo-continuum level. The ORFEUS spectrum, made available to us by D. Cohen, is a 15 point rebinned spectrum. Also in this case the signal of the UVSTAR spectrum is higher than that of both EUVE and ORFEUS spectra. The discrepancy is probably related to the UVSTAR flux calibration in the EUV channel that,

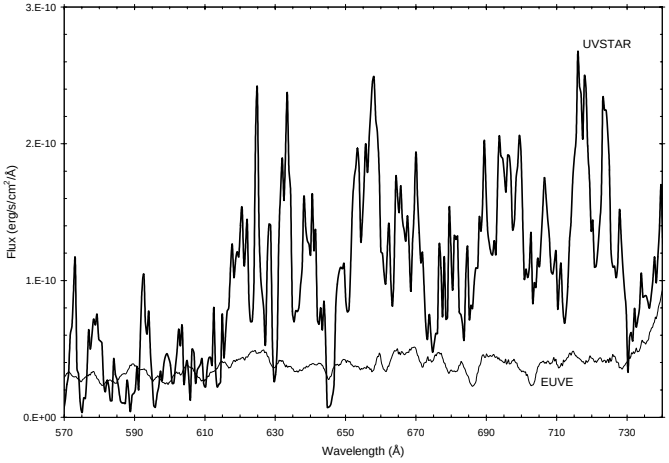

Fig. 4. The calibrated STS 95 UVSTAR spectra (thick lines) compared with EUVE spectrum (medium line).

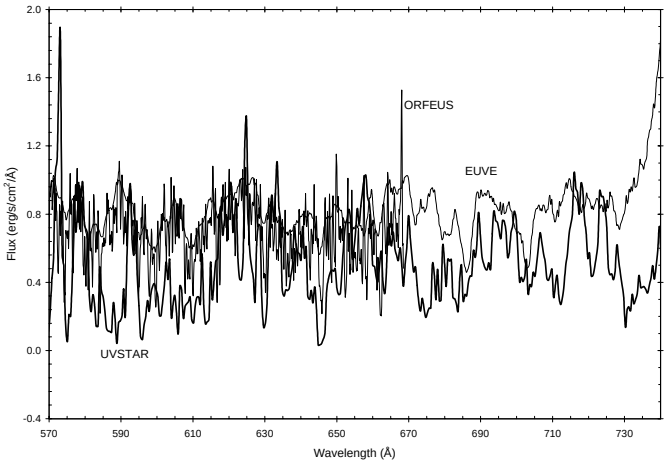

Fig. 5. The normalized STS 95 UVSTAR spectra (thick lines) compared with EUVE (medium line) and ORFEUS (thin line) spectra.

being an extrapolation of the FUV calibration, could be inaccurate, especially at very short wavelengths.

4. Spectral analysis

4.1. FUV variability

Here we describe an unexpected pattern of spectral variations of Adara which deserves careful analysis. The UVSTAR FUV spectrum, already shown in Fig. 2, points out that dispersion is larger around two wavelength bands centered at about 960 and 1045 Å. This might indicate intrinsic stellar variability.

In order to verify this hypothesis and derive possible correlation or anti-correlation features in the data, we have developed a procedure based on the following steps:

1. Compute the correlation among the 38 spectra $r(\lambda_j)$ by comparing the counts in each bin $(x_i(\lambda_j),\ i = 1,38,\ j = 1,1024)$ with corresponding counts at a reference point. The reference point has been chosen to be at 1044 Å since around this point the dispersion is maximum: $r(\lambda_j) = \frac{\Sigma_{i=1}^{38}(x_i(\lambda_j)-\bar{x}(\lambda_j))\cdot(x_i(1044)-\bar{x}(1044))}{[\Sigma_{i=1}^{38}(x_i(\lambda_j)-\bar{x}(\lambda_j))^2\cdot\Sigma_{i=1}^{38}(x_i(1044)-\bar{x}(1044))^2)]^{1/2}}$. Correlation is set to zero if the statistical error is larger than the correlation itself;
2. Evaluate, for each of these 1024 correlation values $r(\lambda_j)$, the probability $P(|r_j|)$ that 38 measurements of two un-correlated variables would give a correlation coefficient greater than $r(\lambda_j)$. If $P(|r_j|) \leq 1\%$, the correlation has been called highly significant otherwise it has been set to one;
3. Enhance regions where both dispersion and correlation/anti-correlation are significant by using a correlation parameter $\epsilon(\lambda)$ defined as the relative dispersion times $(1 - P)$.

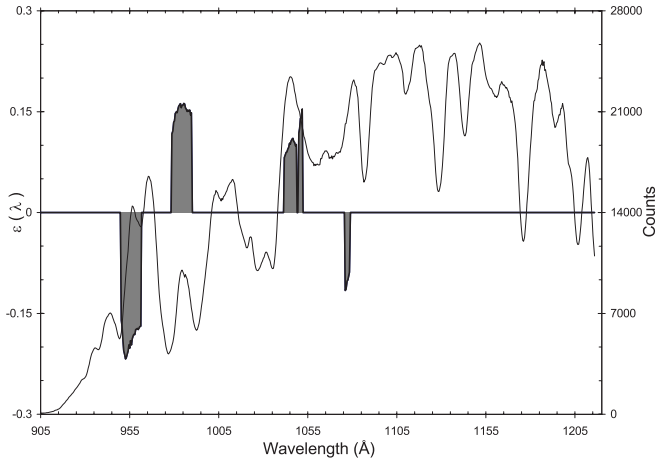

Fig. 6. The distribution of $\epsilon(\lambda)$ (i.e. the relative dispersion times $1 - P$). For clarity sake, correlated and anti-correlated regions are indicated with positive and negative sign respectively. The average spectrum is super-imposed in order to associate the correlated/anti-correlated regions to the spectral features.

Adara FUV spectrum, in counts (thin line), is compared to the correlation parameter $\epsilon(\lambda)$ (filled bands) in Fig. 6; it indicates the existence of four well defined regions, two correlated: in the bands 1040–1052 Å (containing the reference point) and 977–990 Å and two anti-correlated: 1074–1079 Å and 949–962 Å.

On average the time difference between two consecutive images is 16 s, the total observing time being about 11 min. In order to point out possible short time variability effects, we have independently analyzed these four bands as a function of the 38 observing times (corresponding to the 38 spectra). The 38 counts, summed over the band, have been re-normalized on average to one. The four resulting curves are presented in Fig. 7. A Fourier analysis of the four curves indicates the presence of three common main fundamental periods at about 30, 58 and 830 s. Since the four curves exhibit a large correlation, by using a weighted least square fit, the mutual linear correlations between the four curves and the corresponding angular coefficients have been computed, the results are given in Table 2. The errors are the result of the statistical

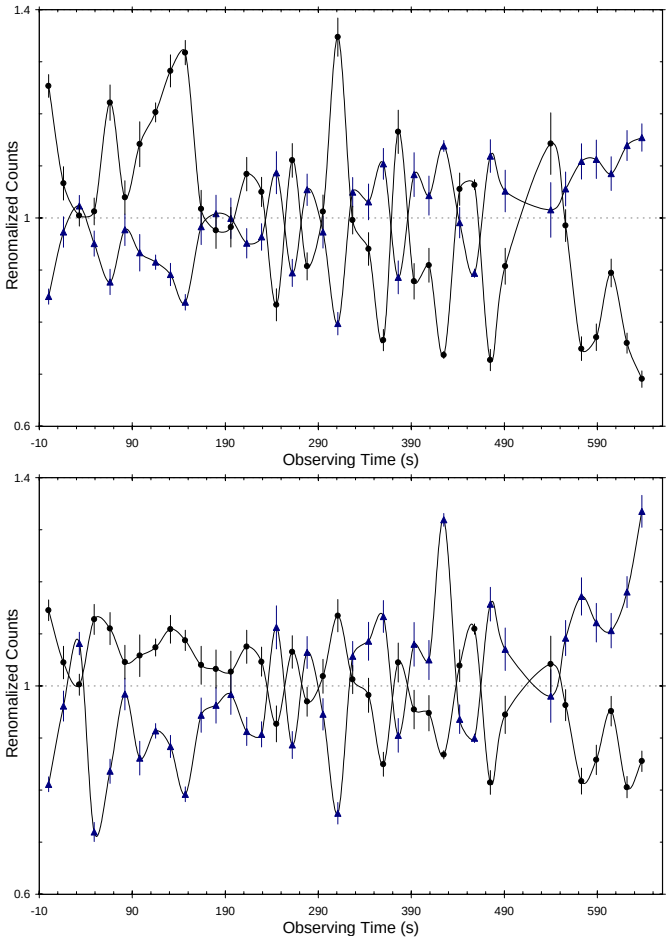

Fig. 7. The re-normalized counts in the four bands as a function of the observing time: 1040–1052 Å (thin line, triangles) and 949–962 Å (thick line, circles) on the top plot, 977–990 Å (thin line, triangles) and 1074–1079 Å (thick line, circles) on the bottom plot. On a single curve each point represents the counts, summed over the corresponding band, of one of the 38 spectra.

and systematic uncertainties on the individual 38 spectra, the systematic error (mainly due to the normalizations among the spectra) giving the dominant contribution. The minimum correlation is 88%: the probability that two uncorrelated measurements give this value with $N = 38$ degree of freedom is well below 0.05%, thus very high significant.

The same procedure has been applied to STS 69 Adara data. The statistics and quality of the data were much poorer than in STS 95 even when choosing the 30 best quality spectra. On average the relative dispersion is of the order of 11% compared to the 8% in STS 95, thus any detection of physical effects has been impossible.

In order to check that the effects observed in STS 95 data are not related to instrumental effects or to data reduction, we have performed two more tests.

First the analysis has been repeated on another set of STS 95 spectra corresponding to the observations of β–Lyrae. According to Hack et al. (1975, 1976, 1977) β–Lyr is a complex system consisting of a B 8 primary star, an

Table 2. Mutual angular coefficients and correlations (square brackets below angular coefficients) between the four data sets: (1) = 1040–1052 Å, (2) = 977–990 Å, (3) = 949–962 Å, (4) = 1074–1079 Å.

	(1)	(2)	(3)	(4)
(1)	1	1.60 ± 0.13	−1.78 ± 0.14	−0.94 ± 0.10
	[100%]	[92%]	[−95%]	[−91%]
(2)	0.63 ± 0.05	1	−1.09 ± 0.11	−0.60 ± 0.06
	[92%]	[100%]	[−88%]	[−91%]
(3)	−0.56 ± 0.04	−0.94 ± 0.07	1	0.58 ± 0.05
	[−95%]	[−88%]	[100%]	[92%]
(4)	−0.89 ± 0.09	−1.68 ± 0.13	1.73 ± 0.15	1
	[−91%]	[−90%]	[92%]	[100%]

unknown companion, an envelope and a disk. The FUV spectrum is dominated by high ionization emission lines (O VI, S VI, N V, S IV, C III, N III, etc.) and by many absorption lines of molecular and atomic hydrogen. The star was observed by UVSTAR on November 7th, 1998 at MET 07/23:20–07/23:30, the total observing time being about 6.5 min. The signal to noise ratio was excellent, larger than 10. We have selected the 12 out of 18 best quality spectra; the quality of the tracking was good but not of the same order as for Adara. We have built a correlation plot which does not show any well-defined region of correlation or anti-correlation. As expected, the only band where the correlation is larger than the error is the one containing the reference point.

The second test has been performed on the two sets of spectra: ϵ CMa and β–Lyr. The aim is to reproduce the observed dispersions and correlations by starting from the average spectra and varying the counts randomly in different parts of the spectra accordingly to the statistical error. If the effect we see is purely statistical, these procedure should reproduce it. The resulting dispersion well reproduces the observed β–Lyr spectrum while the spectrum of ϵ CMa shows defined regions where neither the statistical errors or the simulated variations reproduce the total observed dispersion; the resulting correlations are always negligible. Once more this test excludes a statistical explanation for the observed variability effect.

It is interesting to note that 1) the time scale of these variations appears to be of the order of a minute, i.e. very short for a wide-spread atmospheric effect, and 2) the variability pattern involves bands which do not seem to be related to any particular ionic species: the 949–962 Å band contains, as interesting lines, Lyman–δ, the resonance line of P IV and He II 959 Å; in the 977–990 Å band we have the resonance lines of C III 977 Å, several resonance lines of chlorine and marginally the resonance lines of N III; no prominent spectral lines are reported in the other two bands from 1040 to 1052 Å and from 1074–1079 Å (see Stalio & Selvelli 1975).

FUV spectrum changes in ν Eri, a B2 III β Cephei star having spectral characteristics similar to Adara, was described in detail by Porri et al. (1994) using Voyager UVS

low resolution data. The authors measured the 930–1180 Å and 1350–1500 Å integrated fluxes as a function of phase calculated using the period of 0.1735089 days reported in the literature. No evidence is found of time scales as short as in Adara. Straight phase correlations are obtained in the two bands and with the absorption equivalent widths of the C IV 1548–1551 Å resonance doublet measured from high resolution IUE spectra. Vice-versa, a spectral feature related to the C III 977 Å line (Voyager data) is half a cycle out of phase with C IV and the continuum fluxes. This behavior is explained by the authors as an effect of photospheric temperature changes with pulsational phase.

In Adara, we note that two of the four analyzed bands are located on the short and long wavelength side of the C III 977 Å. We also note that the band from 1040 to 1052 Å is near the long wavelengths side of the O VI resonance doublet. Expressing the band width in velocities relative to C III and O VI, one notices that: 1) the anti-correlated variations (949 to 962 Å) extend from approximately −4600 to −8600 km s^{-1} from C III; 2) the correlated variations extend respectively from 0 to +4000 km s^{-1} (C III) and from 700 to 4100 km s^{-1} (O VI, 1033.8 Å). C III and O VI are major features in the FUV spectra of early type stars; they are are well recognized stellar wind lines which sometimes are concomitantly present in the spectra (Stalio & Gregorio 2000). In the Adara spectrum, at UVSTAR resolution, they are not seen as wind lines probably because of the absence of a mass flux large enough to produce P Cygni profiles. Our observations possibly suggest that they are influencing that part of the atmosphere where the ionic density is not large enough to produce detectable standard spectroscopic signatures. Their presence could only be seen by means of flux variations. The measured time scales favor a restricted area where these changes occur; the different ionization potentials of C III and O VI might explain the fact that we don't see the anti-correlated absorption in O VI. It remains to explain the origin of the anti-correlated feature at λ 1074–1079. It could be related to two S IV resonance lines at 1073 Å or, if the wind interpretation is correct, to an unidentified line at λ 1100 Å which is a characteristic strong feature of early-type stars (Stalio & Selvelli 1975; Walborn & Bohlin 1996).

4.2. Line identification

Table 3 lists the major identified stellar lines of the FUV spectrum. In the EUV band the huge number of lines contributing to the line spectrum makes standard methods of line identification really difficult. In Tables 4 and 5 we give a list of selected lines of elements which seem to be definitely present (only light and abundant elements have been considered).

Both in the FUV and EUV spectra there are no indications of high velocity spectral features, even if the high energies involved suggest that we are sampling a region where the photosphere might co-exist with the wind and where it acquires energy and acceleration.

Table 3. Identified FUV lines: wavelengths (Å), transition probabilities A_{ki} (10^8 s^{-1}) and energies (eV). In parenthesis relative intensity is given when A_{ki} is not available.

Elem.	Wavel.	A_{ki}	$E_i - E_k$	configurations	terms
C II*	1036.34	7.6	0.0–12.0	$2s^2(1S)2p–2s2p^2$	$^2P°–^2S$
C II*	1037.02	15.2	0.0–12.0	$2s^2(1S)2p–2s2p^2$	$^2P°–^2S$
C III	977.02	17.7	0.0–12.7	$2s^2–2s(^2S)2p$	$^1S–^1P°$
C III	1175.71	9.9	6.5–17.0	$2s(^2S)2p–2p^2$	$^3P°–^3P$
C III	1175.99	13.1	6.5–17.0	$2s(^2S)2p–2p^2$	$^3P°–^3P$
C III	1176.37	5.5	6.5–17.0	$2s(^2S)2p–2p^2$	$^3P°–^3P$
H I	937.80	0.2	0.0–13.2	1s–6p	$^2S–^2P°$
H I	949.74	0.3	0.0–13.1	1s–5p	$^2S–^2P°$
H I	972.54	0.7	0.0–12.7	1s–4p	$^2S–^2P°$
H I	1025.72	1.7	0.0–12.1	1s–3p	$^2S–^2P°$
H I	1215.67	6.3	0.0–10.2	1s–2p	$^2S–^2P°$
He II	992.36	(8)			
He II	1025.27	(15)			
He II	1084.94	(30)			
N II*	1083.99	2.2	0.0–11.4	$2s^2(1S)2p^2–2s(^2S)2p^3$	$^3P–^3D°$
N II*	1084.58	2.9	0.0–11.4	$2s^2(1S)2p^2–2s(^2S)2p^3$	$^3P–^3D°$
N II*	1085.70	3.9	0.0–11.4	$2s^2(1S)2p^2–2s(^2S)2p^3$	$^3P–^3D°$
N III	989.80	4.2	0.0–12.5	$2s^2(1S)2p–2s2p^2$	$^2P°–^2D$
N III	991.58	5.0	0.0–12.5	$2s^2(1S)2p–2s2p^2$	$^2P°–^2D$
P IV	950.66	39.4	0.0–13.0	$3s^2–3s3p$	$^1S–^1P°$
S III	1021.11	(150)	0.1–12.2	$3s^23p^2–3s3p^3$	$^3P–^3P°$
S III	1021.32	(150)	0.1–12.2	$3s^23p^2–3s3p^3$	$^3P–^3P°$
S III	1077.16	(150)	1.4–12.9	$3s^23p^2–3s^23p3d$	$^1D–^1D°$
S III	1190.20	9.6	0.0–10.4	$3s^23p^2–3s3p^3$	$^3P–^3D°$
S III	1194.06	13.0	0.0–10.4	$3s^23p^2–3s3p^3$	$^3P–^3D°$
S III	1194.45	7.1	0.0–10.4	$3s^23p^2–3s3p^3$	$^3P–^3D°$
S III	1200.97	17.0	0.1–10.4	$3s^23p^2–3s3p^3$	$^3P–^3D°$
S III	1201.73	4.2	0.1–10.4	$3s^23p^2–3s3p^3$	$^3P–^3D°$
S IV	1062.66	17.0	0.0–11.7	$3s^2(1S)3p–3s3p^2$	$^2P°–^2D$
S IV	1072.97	20.0	0.1–11.7	$3s^2(1S)3p–3s3p^2$	$^2P°–^2D$
S IV	1073.52	3.3	0.1–11.7	$3s^2(1S)3p–3s3p^2$	$^2P°–^2D$
Si III	994.79	7.9	6.6–19.0	3s3p–3s4s	$^3P°–^3S$
Si III	997.39	13.1	6.6–19.0	3s3p–3s4s	$^3P°–^3S$
Si III	1108.36	16.2	6.5–17.7	3s3p–3s3d	$^3P°–^3D$
Si III	1109.94	12.1	6.6–17.7	3s3p–3s3d	$^3P°–^3D$
Si III	1109.97	21.7	6.6–17.7	3s3p–3s3d	$^3P°–^3D$
Si III	1113.20	7.2	6.6–17.7	3s3p–3s3d	$^3P°–^3D$
Si III	1113.23	28.7	6.6–17.7	3s3p–3s3d	$^3P°–^3D$
Si III	1140.55	22.0	16.1–27.0	$3p^2–3p3d$	$^3P–^3D°$
Si III	1141.58	30.0	16.1–27.0	$3p^2–3p3d$	$^3P–^3D°$
Si III	1142.29	16.0	16.1–27.0	$3p^2–3p3d$	$^3P–^3D°$
Si III	1144.31	39.0	16.1–27.0	$3p^2–3p3d$	$^3P–^3D°$
Si III	1144.96	9.7	16.1–27.0	$3p^2–3p3d$	$^3P–^3D°$
Si III	1155.00	7.5	16.1–26.8	$3p^2–3p3d$	$^3P–^3P°$
Si III	1155.96	22.0	16.1–26.8	$3p^2–3p3d$	$^3P–^3P°$
Si III	1160.25	9.1	16.1–26.8	$3p^2–3p3d$	$^3P–^3P°$
Si III	1161.58	16.0	16.1–26.8	$3p^2–3p3d$	$^3P–^3P°$
Si III	1206.50	25.9	0.0–10.3	$3s^2–3s3p$	$^1S–^1P°$
Si III	1206.56	48.9	10.3–20.6	3s3p–3s3d	$^1P°–^1D$
Si III	1207.52	19.0	15.2–25.4	$3p^2–3p3d$	$^1D–^1D°$
Si IV	1066.61	39.1	19.9–31.5	3d–4f	$^2D–^2F°$
Si IV	1066.65	36.5	19.9–31.5	3d–4f	$^2D–^2F°$
Si IV	1122.49	20.5	8.8–19.9	3p–3d	$^2P°–^2D$
Si IV	1128.34	24.2	8.9–19.9	3p–3d	$^2P°–^2D$

* Major ISM contribution.

5. The model atmosphere analysis

Several model atmosphere analyses of Adara have found that the observed flux longward of 912 Å agrees well with models, while that below 912 Å is larger by about one order of magnitude than the predicted one. This discrepancy has been ascribed to an unexpected large EUV flux. Cassinelli et al. (1995) showed that hydrostatic, plane-parallel, line blanketed models, both in LTE (Kurucz 1992) and in non-LTE (Hubeny & Lanz 1995), are unable to reproduce the Adara EUV flux. Non-LTE spherical models including winds but neglecting metal line-blanketing (Najarro et al. 1996) also failed to reproduce

Table 4. Identified EUV lines: wavelengths (Å), transition probabilities A_{ki} (10^8 s^{-1}) and energies (eV). In parenthesis relative intensity is given when A_{ki} is not available.

	Wavel.	A_{ki}	E_i-E_k	configurations	terms
C II	595.02	13.3	0.0–20.8	$2s^2(^1S)2p–2s^2(^1S)4d$	$^2P^\circ–^2D$
C II	651.27	29.3	5.3–24.4	$2s2p^2–2s2p(^3P^\circ)3d$	$^4P–^4D^\circ$
C II	651.35	41.9	5.3–24.4	$2s2p^2–2s2p(^3P^\circ)3d$	$^4P–^4D^\circ$
C II	687.05	23.7	0.0–18.0	$2s^2(^1S)2p–2s^2(^1S)3d$	$^2P^\circ–^2D$
C II	687.35	28.4	0.0–18.0	$2s^2(^1S)2p–2s^2(^1S)3d$	$^2P^\circ–^2D$
C II	809.68	13.5	9.3–24.6	$2s2p^2–2s2p(^3P^\circ)3d$	$^2D–^2D^\circ$
N II	582.16	28.5	1.9–23.2	$2s^2(^1S)2p^2–2s^22p(^2P^\circ)3d$	$^1D–^1D^\circ$
N II	644.84	36.4	0.0–19.2	$2s^2(^1S)2p^2–2s(^2S)3p^3$	$^3P–^3S^\circ$
N II	645.18	60.7	0.0–19.2	$2s^2(^1S)2p^2–2s(^2S)3p^3$	$^3P–^3S^\circ$
N II	660.29	36.9	1.9–20.7	$2s^2(^1S)2p^2–2s(^2S)3p^3$	$^1D–^1P^\circ$
N II	671.39	7.4	0.0–18.5	$2s^2(^1S)2p^2–2s^22p(^2P^\circ)3s$	$^3P–^3P^\circ$
N II	746.98	38.5	1.9–18.5	$2s^2(^1S)2p^2–2s^22p(^2P^\circ)3s$	$^1D–^1P^\circ$
N II	775.97	30.8	1.9–17.9	$2s^2(^1S)2p^2–2s^22p(^2P^\circ)3s$	$^1D–^1D^\circ$
O II	580.97	13.0	5.0–26.4	$2s^22p^3–2s2p^4$	$^2P^\circ–^2P$
O II	600.59	4.7	5.0–25.7	$2s^22p^3–2s^22p^2(^1D)3s$	$^2P^\circ–^2D$
O II	616.30	31.1	3.3–23.4	$2s^22p^3–2s^22p^2(^1D)3s$	$^2D^\circ–^2P$
O II	617.06	34.3	3.3–23.4	$2s^22p^3–2s^22p^2(^1D)3s$	$^2D^\circ–^2P$
O II	644.15	34.8	5.0–24.3	$2s^22p^3–2s2p^4$	$^2P^\circ–^2S$
O II	644.16	17.9	5.0–24.3	$2s^22p^3–2s2p^4$	$^2P^\circ–^2S$
O II	672.95	4.8	5.0–23.4	$2s^22p^3–2s^22p^2(^1D)3s$	$^2P^\circ–^2P$
O II	718.50	19.0	3.3–20.6	$2s^22p^3–2s2p^4$	$^2D^\circ–^2D$
O II	718.57	18.5	3.3–20.6	$2s^22p^3–2s2p^4$	$^2D^\circ–^2D$
O II	796.68	2.0	5.0–20.6	$2s^22p^3–2s2p^4$	$^2P^\circ–^2D$
O II	832.76	8.7	0.0–14.9	$2s^22p^3–2s2p^4$	$^4S^\circ–^4P$
O II	833.33	8.7	0.0–14.9	$2s^22p^3–2s2p^4$	$^4S^\circ–^4P$
O II	834.47	8.6	0.0–14.9	$2s^22p^3–2s2p^4$	$^4S^\circ–^4P$
S II	594.47	(11)	0.0–20.9	$3s^23p^3–3s^23p^2(^3P)5d$	$^4S^\circ–^4P$
S II	640.42	(12)	0.0–19.4	$3s^23p^3–3s^23p^2(^3P)4d$	$^4S^\circ–^4P$
S II	640.90	(13)	0.0–19.3	$3s^23p^3–3s^23p^2(^3P)4d$	$^4S^\circ–^4P$
S II	641.77	(15)	0.0–19.3	$3s^23p^3–3s^23p^2(^3P)4d$	$^4S^\circ–^4P$
S II	655.22	(11)	1.8–20.8	$3s^23p^3–3s^23p^2(^1D)4d$	$^2D^\circ–^2D$
S II	655.22	(11)	1.8–20.8	$3s^23p^3–3s^23p^2(^1D)4d$	$^2D^\circ–^2D$
S II	764.42	(11)	0.0–16.2	$3s^23p^3–3s^23p^2(^3P)3d$	$^4S^\circ–^4P$
S II	765.68	(12)	0.0–16.2	$3s^23p^3–3s^23p^2(^3P)3d$	$^4S^\circ–^4P$

Table 5. Identified EUV lines: wavelengths (Å), transition probabilities A_{ki} (10^8 s^{-1}) and energies (eV). In parenthesis relative intensity is given when A_{ki} is not available.

	Wavel.	A_{ki}	E_i-E_k	configurations	terms
N III	685.00	9.6	0.0–18.1	$2s^2(^1S)2p–2s2p^2$	$^2P^\circ–^2P$
N III	685.52	38.3	0.0–18.1	$2s^2(^1S)2p–2s2p^2$	$^2P^\circ–^2P$
N III	685.82	45.4	0.0–18.1	$2s^2(^1S)2p–2s2p^2$	$^2P^\circ–^2P$
N III	686.34	19.5	0.0–18.1	$2s^2(^1S)2p–2s2p^2$	$^2P^\circ–^2P$
N III	763.33	9.6	0.0–16.2	$2s^2(^1S)2p–2s2p^2$	$^2P^\circ–^2S$
N III	764.35	18.5	0.0–16.2	$2s^2(^1S)2p–2s2p^2$	$^2P^\circ–^2S$
N III	771.90	16.4	7.1–23.2	$2s2p^2–2p^3$	$^4P–^4S^\circ$
N III	772.38	24.5	7.1–23.2	$2s2p^2–2p^3$	$^4P–^4S^\circ$
N III	772.89	20.9	12.5–28.6	$2s2p^2–2p^3$	$^2D–^2P^\circ$
N III	772.96	23.4	12.5–28.6	$2s2p^2–2p^3$	$^2D–^2P^\circ$
N IV	765.15	23.2	0.0–16.2	$2s^2–2s(^2S)2p$	$^1S–^1P^\circ$
O III	599.59	54.1	2.5–23.2	$2s^22p^2–2s2p^3$	$^1D–^1D^\circ$
O III	702.34	6.1	0.0–17.7	$2s^22p^2–2s2p^3$	$^3P–^3P^\circ$
O III	702.84	18.3	0.0–17.7	$2s^22p^2–2s2p^3$	$^3P–^3P^\circ$
O III	702.90	4.5	0.0–17.7	$2s^22p^2–2s2p^3$	$^3P–^3P^\circ$
O III	703.85	7.5	0.0–17.7	$2s^22p^2–2s2p^3$	$^3P–^3P^\circ$
O III	703.85	13.7	0.0–17.7	$2s^22p^2–2s2p^3$	$^3P–^3P^\circ$
O III	833.75	4.6	0.0–14.9	$2s^22p^2–2s2p^3$	$^3P–^3D^\circ$
O III	835.29	6.0	0.0–14.9	$2s^22p^2–2s2p^3$	$^3P–^3D^\circ$
O IV	609.83	24.0	0.0–20.4	$2s^2(^1S_\circ)2p–2s2p^2$	$^2P^\circ–^2S$
O IV	616.95	26.0	15.7–35.8	$2s2p^2–2p^3$	$^2D–^2P^\circ$
O IV	617.04	28.9	15.7–35.8	$2s2p^2–2p^3$	$^2D–^2P^\circ$
O IV	625.13	21.3	8.9–28.7	$2s2p^2–2p^3$	$^4P–^4S^\circ$
O IV	625.85	31.9	8.9–28.7	$2s2p^2–2p^3$	$^4P–^4S^\circ$
O IV	779.82	13.1	15.7–31.6	$2s2p^2–2p^3$	$^2D–^2D^\circ$
O IV	779.91	13.6	15.7–31.6	$2s2p^2–2p^3$	$^2D–^2D^\circ$
O IV	790.20	7.1	0.0–15.7	$2s^2(^1S_\circ)2p–2s2p^2$	$^2P^\circ–^2D$
O V	629.73	28.7	0.0–19.7	$2s^2–2s(^2)2p$	$^1S–^1P^\circ$
O V	758.68	5.5	10.2–26.5	$2s(^2S)2p–2p^2$	$^3P^\circ–^3P$
O V	760.45	16.5	10.2–26.5	$2s(^2S)2p–2p^2$	$^3P^\circ–^3P$
P IV	823.18	26.3	8.4–23.5	3s3p–3s3d	$^3P^\circ–^3D$
P IV	824.73	35.2	8.4–23.5	3s3p–3s3d	$^3P^\circ–^3D$
P IV	827.93	46.4	8.5–23.5	3s3p–3s3d	$^3P^\circ–^3D$
P V	865.45	31.0	11.0–25.3	3p–3d	$^2P^\circ–^2D$
P V	871.39	36.2	11.1–25.3	3p–3d	$^2P^\circ–^2D$
S III	677.73	(20)	0.0–18.3	$3s^23p^2–3s^23p3d$	$^3P–^3D^\circ$
S III	678.46	(30)	0.0–18.3	$3s^23p^2–3s^23p3d$	$^3P–^3D^\circ$
S III	700.29	(20)	0.0–17.7	$3s^23p^2–3s^23p3d$	$^3P–^3P^\circ$
S III	702.78	(35)	0.1–17.7	$3s^23p^2–3s^23p3d$	$^3P–^3P^\circ$
S III	710.96	(30)	1.4–18.8	$3s^23p^2–3s3p^3$	$^1D–^1D^\circ$
S III	725.86	(25)	0.0–17.1	$3s^23p^2–3s3p^3$	$^3P–^3S^\circ$
S III	728.69	(35)	0.1–17.1	$3s^23p^2–3s3p^3$	$^3P–^3S^\circ$
S IV	661.40	(17)	0.1–18.9	$3s^2(^1S)3p–3s^2(^1S)3d$	$^2P^\circ–^2D$
S IV	661.45	(17)	0.1–18.9	$3s^2(^1S)3p–3s^2(^1S)3d$	$^2P^\circ–^2D$
S IV	744.90	(16)	0.0–16.6	$3s^2(^1S)3p–3s3p^2$	$^2P^\circ–^2P$
S IV	748.39	(15)	0.0–16.6	$3s^2(^1S)3p–3s3p^2$	$^2P^\circ–^2P$
S IV	750.22	(16)	0.1–16.6	$3s^2(^1S)3p–3s3p^2$	$^2P^\circ–^2P$
S IV	753.76	(18)	0.1–16.6	$3s^2(^1S)3p–3s3p^2$	$^2P^\circ–^2P$
S IV	809.66	(16)	0.0–15.3	$3s^2(^1S)3p–3s3p^2$	$^2P^\circ–^2S$
S IV	815.94	(15)	0.1–15.3	$3s^2(^1S)3p–3s3p^2$	$^2P^\circ–^2S$
Si IV	645.76	7.0	19.9–39.1	3d–6f	$^2D–^2F^\circ$
Si IV	749.94	14.5	19.9–36.4	3d–5f	$^2D–^2F^\circ$
Si IV	749.94	13.5	19.9–36.4	3d–5f	$^2D–^2F^\circ$
Si IV	818.13	24.4	8.9–24.1	3p–4s	$^2P^\circ–^2S$

the EUV flux of Adara. The non-LTE spherical models of Schaerer & de Koter (1997), which include both stellar winds and line opacity, provide only an artificial agreement with the observations because they do not include line broadening thus restricting the blanketing effect. All the above mentioned models probably fail because they do not predict either the temperature structure or the level populations in the Lyman continuum-forming layers. This is probably related to the presence of stellar winds in the sub-sonic region of the outer atmosphere (Najarro et al. 1996; Schaerer & de Koter 1997) or to X–ray heating mechanisms (Cohen et al. 1996). As noted by Cassinelli et al. (1995), 1) in addition to the EUV continuum excess, this star exhibits a slight mid–IR excess (of the order of 10%) in the band 10–15 μm with respect to a classical Kurucz model, 2) the IR continuum is formed in the same physical layers as the Lyman continuum, 3) these layers are dominated by thermal processes and a local temperature excess of 2000 K would agree with both the Lyman and mid–IR continua (Cassinelli et al. 1995).

Recently, Aufdenberg et al. (1999) generated a hydrostatic, spherical, non-LTE, metal blanketed model atmosphere of Adara which they affirmed to be able to reproduce both the observed EUV continuum and the flux distribution longward of 912 Å to 25 000 Å. The completeness of the computations has a significant effect on the temperature structure of the model which results in higher values at the formation depth of the H and He I Lyman continua. The agreement between this model and the data could imply that the behavior of Adara is not peculiar, thus representing a typical B2 II star. Adara is an ideal object for testing advanced model atmosphere codes because of the different depth in the atmosphere from where the EUV, UV/visible and IR radiation originates.

5.1. Interstellar absorption and reddening

Both interstellar absorption in the stellar direction and reddening $E(B-V)$ have to be considered when the whole observed energy distribution, from EUV to infrared, has to be compared with models.

The interstellar H I column density N(H I) in the Adara direction was estimated by Cassinelli et al. (1995) to be about 1×10^{18} cm^{-2}, while Gry & Dupin (1998) determined a value lower than 4×10^{17} cm^{-2} and Gry & Jenkins (2001) found that it lies between $(6.0 \pm 1.2) \times 10^{17}$ cm^{-2} and $(9.0 \pm 2.0) \times 10^{17}$ cm^{-2}. Even assuming the highest value for N(H I), the corresponding $E(B-V)$ becomes negligible when the relation $E(B-V) = N(\mathrm{H\,I})/5.8 \times 10^{21}$ (Binney & Marrifield 1998) is used. Therefore, the Adara observed energy distribution longward of the Lyman discontinuity does not require any reddening correction when it is compared with the computed energy distributions.

In order to correct the EUV data for the interstellar H I absorption we used the photo-inization cross section of neutral hydrogen $\sigma(\lambda)_{\mathrm{H\,I}}$ from Rumph et al. (1994). The corrected flux is therefore: $F_{\mathrm{corr}}(\lambda) = F_{\mathrm{obs}}(\lambda)/\mathrm{e}^{-\sigma(\lambda)_{\mathrm{H\,I}} N(\mathrm{H\,I})}$.

5.2. Model parameters T_{eff} and log g

We adopted as Adara parameters those of the model atmosphere which best reproduces the visible energy distribution.

The observed visible energy distribution was taken from Breger (1976), in particular we used the observations from Davis & Webb (1974) because they cover the largest wavelength range among the spectrophotometric observations of Adara collected by Breger.

Computed energy distributions are based on ATLAS9 models (Kurucz 1993b) computed for [M/H] = 0.0 and a microturbulent velocity $\xi = 8$ km s^{-1}. In fact, Gies & Lambert (1992) derived for Adara $\xi = 17.8$ km s^{-1} from an LTE analysis of the visible spectrum and $\xi = 11.5$ km s^{-1} from a NLTE analysis. Because there are no opacity distribution functions computed for ξ larger than 8 km s^{-1}, we used ATLAS9 models computed for the highest available value of ξ.

For $E(B-V) = 0.0$, the observed energy distribution was best fitted by the model having parameters $T_{\mathrm{eff}} = 21\,500$ K, log $g = 3.2$. We note that the use of models computed for $\xi = 2$ km s^{-1} gives $T_{\mathrm{eff}} = 22\,100$ K, log $g = 3.2$, namely the gravity does not change with ξ, but T_{eff} increases when ξ decreases.

All the above comparisons between observed and computed fluxes were made by normalizing observations and computations at 5556 Å. The observed normalized energy distribution was then converted to absolute flux by assuming the Hayes & Latham (1975) calibration for Vega. The absolute flux at earth f_λ(obs) was converted to absolute flux at the star surface F_λ(obs) by means of the relation $F_\lambda(\mathrm{obs}) = (206\,265/(\theta/2))^2 f_\lambda(\mathrm{obs})$, where θ is the angular diameter. The value $\theta = 0.76$ mas gives the best agreement between the observed flux F_λ(obs) and the computed flux $F_\lambda(\mathrm{calc}) = 4\pi H_\nu c/\lambda^2$, where the Eddington flux H_ν is the output of the ATLAS9 code.

5.3. Comparison of the fluxes in the 500–1250 Å range with model predictions

Figures 8 and 9 compare the absolute flux observed by UVSTAR in the range 500–1250 Å with the ATLAS9 flux computed for $T_{\mathrm{eff}} = 21\,500$ K, log $g = 3.2$, [M/H] = 0.0, $\xi = 8$ km s^{-1}. The fluxes are in absolute flux units erg cm^{-2} s^{-1} Å^{-1} at the star surface and are plotted as logarithms. We assumed $\theta = 0.76$ mas as angular diameter. Figure 8 is for a neutral hydrogen column density N(H I) $= 5 \times 10^{17}$ cm^{-2}. Figures 9 is for N(H I) $= 1 \times 10^{17}$ cm^{-2}. The lower value for N(H I) removes the discontinuity at 916 Å (Fig. 8) between the EUV and FUV UVSTAR fluxes. For N(H I) $= 1 \times 10^{17}$ cm^{-2} the levels of the observed and computed fluxes are comparable, but their shape is different.

Figures 10 and 11 show that when the ATLAS9 model is replaced by the Aufdenberg et al. (1999) model for Adara, the quality of the agreement between observations and computations does not change. The Aufdenberg et al. model has parameters $T_{\mathrm{eff}} = 21\,750$ K, log $g = 3.5$, $\xi = 2$ km s^{-1}, [M/H] = 0.0. For the comparisons shown in Figures 10 and 11 we adopted $\theta = 0.77$ mas, which is the angular diameter adopted by Aufdenberg et al.

These results, together with the comparison of the EUV observations with those from EUVE (Sect. 3.3), further support the possibility of uncertainties in the absolute flux calibration of the EUV channel.

5.4. The line spectrum

We compared the UVSTAR spectra of Adara both with a synthetic spectrum based on the ATLAS9 model computed with parameters $T_{\mathrm{eff}} = 21\,500$ K, log $g = 3.2$, [M/H] = 0.0, $\xi = 8$ km s^{-1} and with the Audenberg et al. spectrum computed with a resolution $\Delta\lambda = 2$ Å. We computed a synthetic spectrum with the SYNTHE code of Kurucz (1993a) by using the line list from Kurucz & Bell (1995). It was broadened for a rotational velocity $v \sin i = 35$ km s^{-1} and for two different instrumental resolutions $\lambda/\Delta\lambda$ equal to 500 and 250. The higher resolution spectrum was compared with the EUV data, while the lower resolution spectrum was compared with the FUV data. Figures 12 to 16 and 17 show the comparison of the EUV and FUV spectra with the synthetic spectra. In Figs. 12 to 16 major identified lines are indicated, errors are only statistical. Since the absolute UVSTAR flux is so different from the model, in order to compare the line shapes, in each wavelength band the synthetic spectrum has been shifted towards the observed spectrum. While Fig. 17 indicates a general good agreement between the observed and computed line spectra, Figs. 12 to 16 point out both the large number of missing lines in the computations and the large difference between the observed and predicted line intensities.

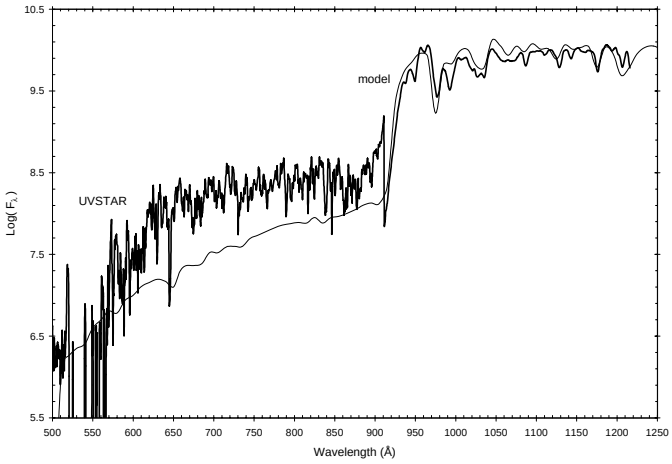

Fig. 8. Comparison between the flux from the ATLAS9 model with parameters $T_{\rm eff} = 21\,500$ K, log $g = 3.2$, [M/H] $= 0.0$, $\xi = 8$ km s^{-1} and the absolute flux from UVSTAR for an angular diameter $\theta = 0.76$ mas and a neutral hydrogen column density $N(\mathrm{H\,I}) = 5 \times 10^{17}$ cm^{-2}.

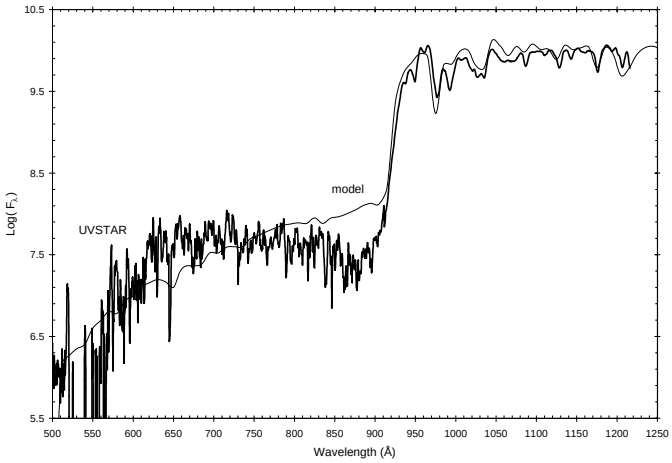

Fig. 9. Comparison between the flux from the ATLAS9 model with parameters $T_{\rm eff} = 21\,500$ K, log $g = 3.2$, [M/H] $= 0.0$, $\xi = 8$ km s^{-1} and the absolute flux from UVSTAR for an angular diameter $\theta = 0.76$ mas and a neutral hydrogen column density $N(\mathrm{H\,I}) = 1 \times 10^{17}$ cm^{-2}.

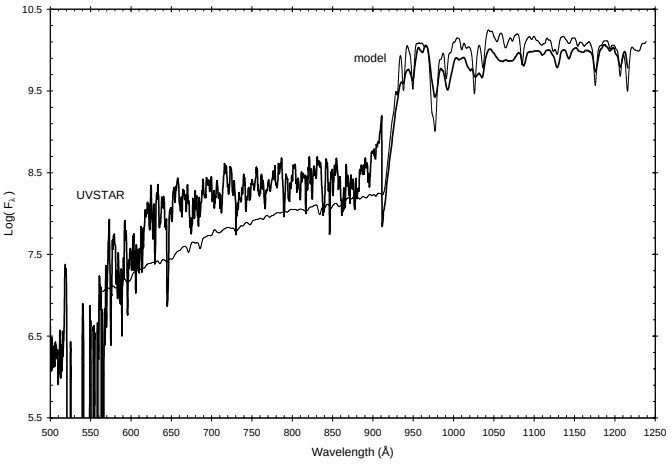

Fig. 10. Comparison between the flux from the Aufdenberg et al. (1999) model with parameters $T_{\rm eff} = 21\,750$ K, log $g = 3.5$, [M/H] $= 0.0$, $\xi = 2$ km s^{-1} and the absolute flux from UVSTAR for an angular diameter $\theta = 0.77$ mas and a neutral hydrogen column density $N(\mathrm{H\,I}) = 5 \times 10^{17}$ cm^{-2}.

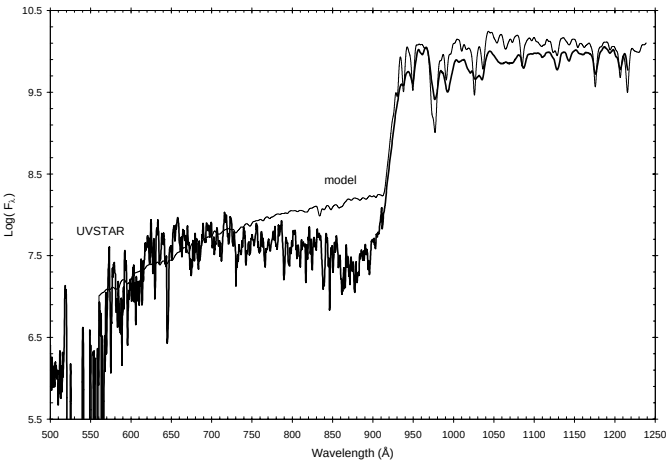

Fig. 11. Comparison between the flux from the Aufdenberg et al. (1999) model with parameters $T_{\rm eff} = 21\,750$ K, log $g = 3.5$, [M/H] $= 0.0$, $\xi = 2$ km s^{-1} and the absolute flux from UVSTAR for an angular diameter $\theta = 0.77$ mas and a neutral hydrogen column density $N(\mathrm{H\,I}) = 1 \times 10^{17}$ cm^{-2}.

6. Conclusions

The main result of this paper is the discovery of extremely rapid flux variations in the four $\lambda\lambda$ 949–962 Å, 977–990 Å, 1040–1052 Å and 1074–1079 Å bands and their counterphase characteristics that is quite unexpected. At this stage we have no explanation for it: this behavior could be related to a new, much faster than typical, form of instabilities occurring in that part HR diagram (β Cephei phenomenon) to which Adara belongs or to some effect related to the region where the stellar winds take energy and acceleration.

The comparison of the UVSTAR spectra with those from other UV experiments has shown that the FUV observations are in good agreement with the Voyager spectra, while the EUV spectra are brighter than the EUVE and ORFEUS spectra. The comparison with models shows the same behaviour. The FUV observations are rather well-reproduced by an ATLAS9 model with parameters $T_{\rm eff} = 21\,500$ K, log $g = 3.2$, [M/H] $= 0.0$, $\xi = 8$ km s^{-1} or by the Aufdenberg et al. (1999) model with parameters $T_{\rm eff} = 21\,750$ K, log $g = 3.5$, [M/H] $= 0.0$, $\xi = 8$ km s^{-1}. Instead, the EUV fluxes have a different shape than the fluxes predicted by the two models and also the line intensity is much stronger in the observations than in the models, so that the comparison of the observed and predicted line spectra is very hard. The conclusion is that either the EUV data reduction suffers from unresolved problems or that the stellar variability has modified the spectra when observed at different epochs. Finally, UVSTAR data favor the presence of a very low column density on the order of 1×10^{17} cm^{-2}.

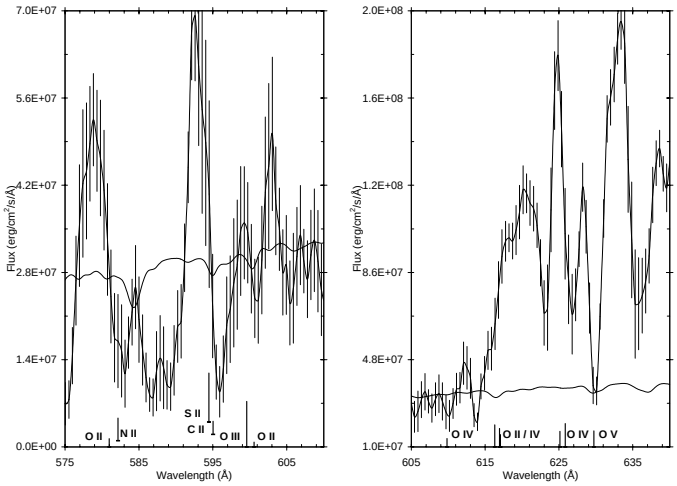

Fig. 12. Comparison between the EUV spectrum with the synthetic spectra (shifted by 2×10^7).

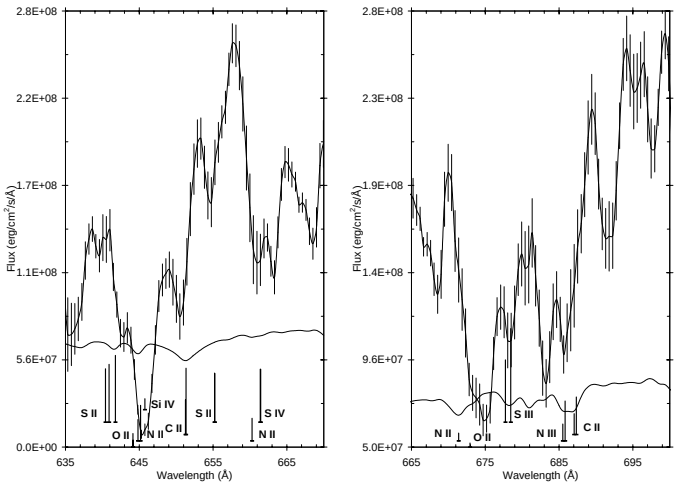

Fig. 13. Comparison between the EUV spectrum with the synthetic spectra (shifted by 5×10^7).

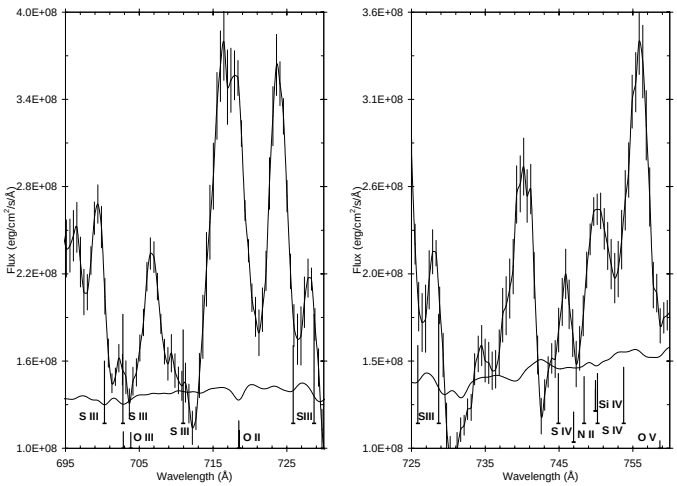

Fig. 14. Comparison between the EUV spectrum with the synthetic spectra (shifted by 1×10^8).

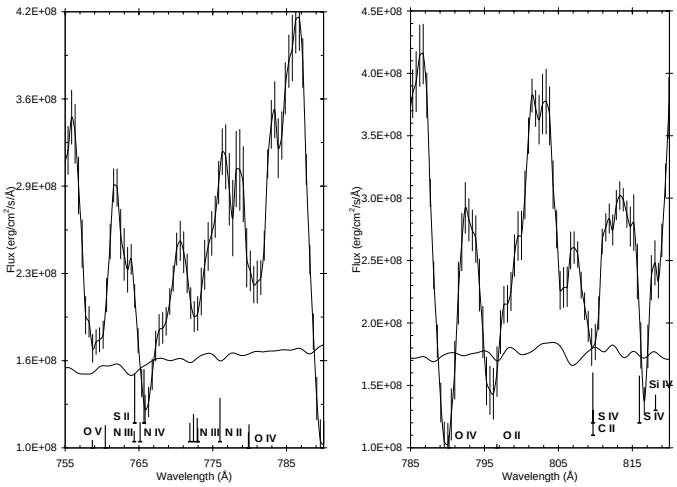

Fig. 15. Comparison between the EUV spectrum with the synthetic spectra (shifted by 1×10^8).

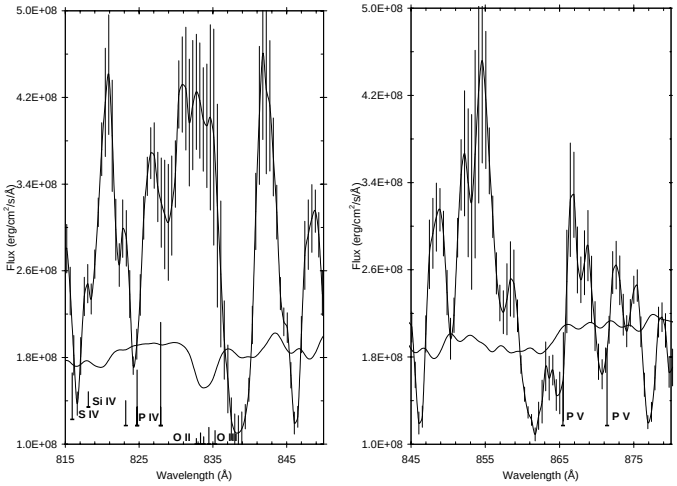

Fig. 16. Comparison between the EUV spectrum with the synthetic spectra (shifted by 1×10^8).

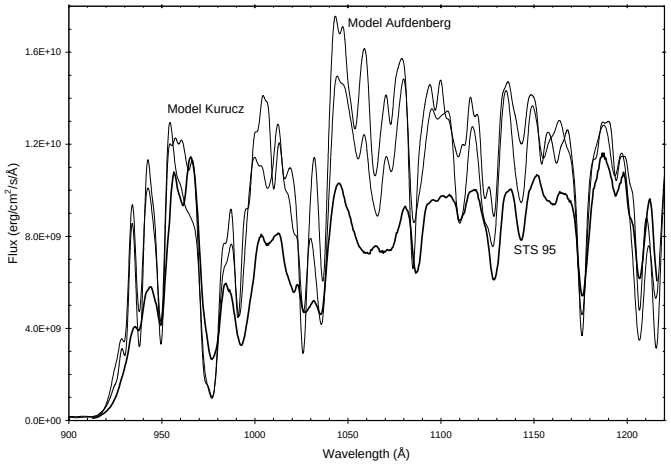

Fig. 17. Comparison between the FUV spectrum with the synthetic spectra. The thick line represents the UVSTAR STS 95 spectrum, the medium and thin lines represent the synthetic spectra, the Kurucz and Aufdenberg models respectively.

UVSTAR has allocated two more missions: one of the main science goals will be to continue and improve the observations of Adara in both EUV and FUV. Observing Adara again in these bands could give important clues for an understanding of the stellar photosphere and wind connection.

Acknowledgements. This work has been performed under ASI (Agenzia Spaziale Italiana) contract. The UVSTAR experiment is a joint collaboration between the Universities of Trieste and Arizona. We thank the CARSO technical staff and in particular Drs. Andrea Bucconi and Paolo Trampus. We also thank the NASA SSPP team and in particular Mr. Tom Dixon and Mr. Gerry Daelemans. We are particularly grateful to prof. Gianrossano Giannini for his contribution in defining the data analysis procedures. We thank also David Cohen for delivering EUVE data and Jason Aufdenberg who provided new Adara model atmospheres.

References

Aufdenberg, J. P., Hauschilat, P. H., & Baron, E. 1999, MNRAS, 302, 599
Binney, H., & Marrifield, M. 1998, Galactic Astronomy, Princeton Series in Astrophysics (Princeton University Press)
Bowyer, S., Lampton, M., Lewis, J., et al. 1996, ApJS, 102, 129
Breger, M. 1976, ApJS, 32, 7
Broadfoot, L. A. 2000, private communication
Buss, R. H. Jr., Allen, M., McCandliss, S., et al. 1994, ApJ, 430, 630
Cassinelli, J. P., Cohen, D. H., MacFarlane, J. J., et al. 1995, ApJ, 932 C, 438
Code, A. D., Bless, R. C., Davis, J., & Brown, R. H. 1976, ApJ, 203, 417
Cohen, D. H., Cooper, R. G., MacFarlaine, J. J., et al. 1996, ApJ, 460, 506
Cohen, D. H., Hurwitz, M., Cassinelli, J. P., & Bowyer, S. 1998, ApJ, 500 L, 511
Cohen, D. H., Cassinelli, J. P., MacFarlaine, J. J., & Owocki, S. P. 2000, Thermal and Ionization Aspects of Flows from Hot Stars: Observations and Theory, Astron. Soci. Pac. Conf. Ser., 204, 81
Davis, J., & Webb, R. J. 1974, MNRAS, 168, 163
De Carlo, F., Stalio, R., Trampus, P., Sandel, B. R., & Sicuranza, G. 1994, Opt. Eng., 33(8), 2738
Drew, J. E., Denby, M., & Hoare, M. G. 1994, MNRAS, 266, 917
ESA 1997, The Hipparcos and Tycho Catalogues, ESA SP–1200, HIP 33579
Gies, D. R., & Lambert, D. L. 1992, ApJ, 387, 673
Gry, C., York, D. G., & Vidal-Madjar, A. 1985, ApJ, 296, 593
Gry, C., Lemonon, L., Vidal-Madjar, A., Lemoine, M., & Ferlet, R. 1995, A&A, 302, 497
Gry, C., & Dupin, O. 1998, LNP, 506, 161G
Gry, C., & Jenkins, E. B. 2001, A&A, 367, 617
Hack, M., Hutchings, J. B., Kondo, Y., et al. 1975, ApJ, 198, 453
Hack, M., Tulloch, M. H., Hutchings, J. B., Kondo, Y., & McCluskey, G. E. 1976, ApJ, 206, 777
Hack, M., Hutchings, J. B., Kondo, Y., & McCluskey, G. E. 1977, ApJS, 34, 565
Hamamatsu Catalogue 1994, MCP Assembly, Technical Information
Hanbury Brown, R., Davis, J., & Allen, L. R. 1974, MNRAS, 167, 121
Hayes, D. L., & Latham, D. W. 1975, ApJ, 197, 593
Hoare, M. G., Drew, J. E., & Denby, M. 1993, MNRAS, 262, L19
Holberg, J. B., Ali, B., Carone, T. E., & Polidan, R. S. 1991, ApJ, 375, 716
Hubeny, I., & Lanz, T. 1995, ApJ, 439, 875
Kruk, J. W., Kimble, R. A., Buss, R. H. Jr., et al. 1997, ApJ, 482, 546
Kurucz, R. L. 1992, Model Atmospheres for Population Synthesis, ed. B. Barbury, & A. Renzini (Dordrecht: Kluwer), 225
Kurucz, R. L. 1993a, SYNTHE Spectrum Synthesis Programs and Line DATA, CD-ROM, No. 18
Kurucz, R. L. 1993b, ATLAS9 Stellar Atmosphere Programs and km s^{-1} grid, CD-ROM, No. 13
Kurucz, R. L., & Bell, B. 1995, Atomic Line List, CD-ROM, No. 23
Morales, C., Trapero, J., Gomez, J. F., et al. 2000, ApJ, 530, 403
Morales, C., Orozco, V., Gomez, J. F., et al. 2001, ApJ, 550
Najarro, F., Kudritzki, R. P., Cassinelli, J., Stahl, O., & Hillier, D. J. 1996, A&A, 306, 892
Porri, A., Stalio, R., Ali, B., Polidan, R. S., & Morossi, C. 1994, ApJ, 424, 401
Rumph, T., Bowyer, S., & Vennes, S. 1994, AJ, 107, 2108
Sandel, B., Broadfoot, L. A., & Stalio, R. 1993, Opt. Eng., 32(12), 3009
Schaerer, D., & de Koter, A. 1997, A&A, 322, 598
Stalio, R., & Salvelli, P. L. 1975, A&AS, 21, 241
Stalio, R., Gregorio, A., & Trampus, P. 1999, UV Astronomy in Italy, J. Ital. Astron. Soc., 70(2), 349
Stalio, R., & Gregorio, A. 2000, Thermal and Ionization Aspects of Flows from Hot Stars: Observations and Theory, Astron. Soc. Pacific Conf. Ser., 204, 81
Struve, O., & Zebergs, V. 1960, ApJ, 132, 87
Trampus, P., Bucconi, A., & Zennaro, G. 1999, Shuttle Small Payloads Symposium, NASA/CP–1999–209476, 261
Trampus, P., Stalio, R., & Cortiglioni, S. 1999, Bridging the Future Space Station and beyond, STAIFF 2000, AIP Conf. Proc., 504, 97
Uesugi, A., & Fukuda, I. 1982, Revised Catalog of Stellar Rotational Velocities, University of Kyoto
Vallerga, J. V., & Welsh, B. Y. 1996, Astrophysics in the Extreme Ultraviolet, ed. S. Bowyer, & R. F. Malina, 277
Walborn, N. R., & Bohlin, R. C. 1996, PASP, 108, 477
Welsh, B. Y. 1991, ApJ, 373, 556